CEAS Aeronautical Journal
https://doi.org/10.1007/s13272-025-00913-3

ORIGINAL PAPER

Validation of high-fidelity aeroelastic simulations with flight test data from DLR Dassault Falcon 2000LX ISTAR

M. Bauer[1] · J. Feldwisch[2] · P. Mühlmann[1] · T. Kirmse[3]

Received: 31 March 2025 / Revised: 29 June 2025 / Accepted: 13 October 2025

Abstract
This paper presents a validation of high-fidelity aeroelastic simulations using experimental data measured on the new DLR research aircraft Dassault Falcon 2000LX ISTAR in the clean cruise configuration during the HighFly flight campaign MaGE (Maneuvers at the Border of the Envelope). The simulations are performed with DLR's multidisciplinary process chains FSAerOpt and UltraFLoads, which combine DLR TAU-Code as a flow solver with MSC Nastran as a structural solver. Steady-state trimmed fluid-structure coupled simulations of five flight points are investigated. The following parameters and data from the simulations and the flight measurements are compared: chordwise wing section pressure distributions, trim variables, and elastic wing deformations. Three pressure distributions on the right wing were measured on the ISTAR aircraft using pMEMS (Micro Electro Mechanical System) sensors, and elastic structural deformations of the left wing were measured using IPCT (Image Pattern Correlation Technique). Finally, the effects of the level of CFD geometry detail, the CFD mesh resolution, and different numerical parameters on the simulation results are discussed.

Keywords CFD validation · Virtual flight testing · Certification by analysis · Simulation-based certification

1 Introduction

1.1 Motivation and long-term vision

The central goal in current aviation research and development is improving aircraft efficiency and reducing the environmental impact of flying. Besides optimizing the flight routes and overall air transport system, the main possible improvements are advances in aircraft aerodynamics, materials, structures, and propulsion systems. To achieve these aircraft improvements while always ensuring flight safety, it is important to accurately and quickly analyze aircraft characteristics such as flight performance, external and internal loads, aeroelasticity phenomena, flight control, and stability with numerical simulation methods. They do not have to be used only at the early stages of development, for example, in the framework of multidisciplinary design optimization (MDO), but also at later stages to create an aircraft digital twin for virtual flight testing and certification by analysis (simulation-based certification) [1–3]. In the future, highly accurate virtual flight tests could partially replace some real certification flight tests that are associated with high costs, time demands, and risks. For example, the testing and certification of the Airbus A350-900 required five test aircraft, over 14 months, and over 2600 flight hours [4]. In the near future, virtual flight tests can support the preparation and optimization of real flight tests and certification campaigns. With virtual flight tests, problems or errors in aircraft design can also be detected at an early development stage. Using high-fidelity methods already in the conceptual and preliminary design stages can be reasonable and beneficial because these stages define about 85% of the total aircraft life-cycle

✉ M. Bauer
Ma.Bauer@dlr.de

J. Feldwisch
Johan.Feldwisch@dlr.de

P. Mühlmann
Philipp.Muehlmann@dlr.de

T. Kirmse
Tania.Kirmse@dlr.de

[1] German Aerospace Center (DLR), Institute of Aerodynamics and Flow Technology, Lilienthalplatz 7, 38108 Brunswick, Germany

[2] German Aerospace Center (DLR), Institute of Aeroelasticity, Bunsenstraße 10, 37073 Göttingen, Germany

[3] German Aerospace Center (DLR), Institute of Aerodynamics and Flow Technology, Bunsenstraße 10, 37073 Göttingen, Germany

Published online: 13 December 2025

costs [5]. Well before the first flight, it can be verified that the new aircraft type is safe and customer(s) requirements such as range, fuel efficiency, noise, take-off, and landing performance are met.

Extensive verification and validation activities must first be carried out to confirm the sufficient accuracy and level of fidelity of the virtual flight test simulations. This creates the necessary confidence and acceptance for the certification authorities and aircraft manufacturers to use these methods for certification by analysis. Virtual flight tests as part of aircraft development digitalization should then enable faster and more cost-effective progress of new technologies toward climate-neutral air transport.

1.2 Transport aircraft maneuver simulations and their validation

Virtual flight testing of transport aircraft can be challenging and complex. Due to lightweight structures and high aspect ratio wings, modern transport aircraft are highly flexible, which leads to strong interactions between the flow and the wing deformation. This means an interaction between the aerodynamic, elastic, and inertial forces, as described by the Collar aeroelastic triangle [6]. In addition, calculating the steady and unsteady aerodynamic loads is challenging because of nonlinear phenomena such as viscous effects in boundary layers, boundary layer separations, flight control surface deflections, shock waves in the transonic regime, and shock wave-boundary layer interactions. The latter can lead to the fast oscillation of the shock wave (buffet) on the wing at higher transonic Mach numbers and angles of attack (Fig. 1, point 5). This means that for dynamic maneuver simulations of free-flying flexible aircraft in the transonic regime, a multidisciplinary approach (aerodynamics with flight control surface modeling, structural dynamics, and flight dynamics) and an unsteady nonlinear high-fidelity solver for aerodynamic analysis (such as URANS) are needed.

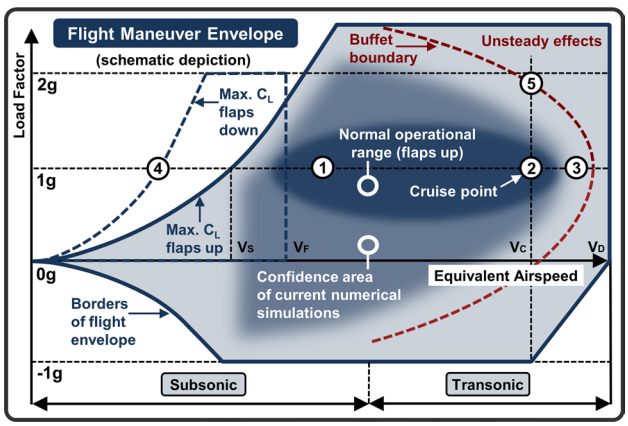

Fig. 1 Flight maneuver envelope of transport aircraft

Continuous developments in high-performance parallel computing, including both hardware and software, have made it possible today to investigate more detailed aircraft geometries described by computer-aided design (CAD) models and to use high-fidelity numerical physical models such as computational fluid dynamics (CFD), computational structural mechanics (CSM), thermodynamic engine models, and flight mechanics models. These models can then be combined into one multidisciplinary process chain. The important task before applying these methods reliably in practice, both in research and industry, is validation, i.e., comparing numerical results with experimental data. Currently, it is not possible to perform proper quantification of accuracy of elastic and highly dynamic flight maneuver simulations via wind tunnel measurements. Therefore, the uncertainty range of these multidisciplinary numerical methods is quantified based on validation data from real flight tests.

Validations of CFD-based numerical simulations developed at DLR for transport aircraft computations using full-scale flight data have been carried out in recent years in the following projects:

- The joint research project HINVA (High Lift Inflight Validation) ran from 2010 to 2015 [7] as part of the German LuFo aeronautical research program. This project aimed to improve the accuracy and reliability of aerodynamic performance predictions of transport aircraft with deployed high-lift devices in the minimum speed and maximum lift flight regimes (Fig. 1, point 4). Numerical simulations based on DLR TAU-Code were compared with flight test data measured on the DLR Airbus A320 ATRA research aircraft [8] and with measurements in the European Transonic Wind Tunnel (ETW) in Cologne, Germany.
- The DLR research project VicToria (Virtual Aircraft Technology Integration Platform) ran from 2016 to 2019. Several real and virtual flight maneuvers of the DLR Airbus A320 research aircraft ATRA [8] were performed to validate flight dynamic simulations. This involved several steady, quasi-steady, and unsteady longitudinal and lateral maneuvers at different altitudes, Mach numbers, load factors, and aircraft configurations (flap settings) [9, 10].
- The DLR research project HighFly [11] was carried out to obtain missing high-quality flight validation data at the flight envelope boundaries at high transonic speeds. The accuracy of numerical simulations in these aerodynamically highly nonlinear areas (Fig. 1, points 3 and 5) is limited or unknown compared to typical cruise flights. The results presented in this paper were created within

the framework of this project. Therefore, this project is described in more detail in the following section.

1.3 DLR research project HighFly

In the DLR research project HighFly (High-Speed Inflight Validation), which ran from 2018 to 2023 [11], the new DLR research aircraft Dassault Falcon 2000LX ISTAR [12], shown in Fig. 2, was used for scientific research for the first time. Falcon 2000LX is a French super-midsize business jet with the following characteristics: certified up to 19 PAX, max. range = 7 400 km, MTOW = 19 142 kg, MMO = 0.85/0.862 and service ceiling = 47 000 ft. Its wings are stiffer than modern transport aircraft wings, but highly dynamic maneuvers are possible due to the aircraft agility.

In the HighFly project, new advanced measurement technologies were developed and evaluated in several ISTAR ground and flight measurement campaigns [13, 14]. Figure 3 presents measurement instruments for the HighFly flight campaign MaGE (Maneuvers at the Border of the Envelope), including a high-precision unsteady wing section pressure measurement based on MEMS (Micro Electro Mechanical System) [15] and a wing deformation measurement based on IPCT (Image Pattern Correlation Technique) [16]. IPCT is a stereoscopic photogrammetry method that uses evaluation algorithms developed for PIV (Particle Image Velocimetry), such as cross-correlation and additional scaling algorithms. IPCT with a multicamera system can measure complex 3D shapes of aircraft during a flight.

The pMEMS measurement system features a set of PCB segments, of which 19 were instrumented with sensors, and some were used as uninstrumented spacers. The length of an instrumented segment is 40 cm, while spacers exist in various lengths. Several segments form a single pressure belt and it is assumed that the transitions between these segments do not have a significant effect on the flow pressure distribution results. The accuracy of the sensors is estimated to be ± 50–100 Pa and the measurement frequency is 100 Hz (suitable for dynamic measurement during flight maneuvers).

The MaGE flight campaign, performed in 2023, contained over 30 flight hours and over 500 maneuvers: trimmed level turns, pull-up and push-down maneuvers, bank-to-bank maneuvers with different roll speeds, level accelerations and decelerations, maneuvers with several elevator pulses or single aileron pulse, and steady heading side slips, covering the complete flight range in the clean configuration (Fig. 4).

The arrangement of the ISTAR instrumentation is unique worldwide. The pressure sensors pMEMS and the acoustic sensors aMEMS were used in the transonic speed range

Fig. 2 DLR research aircraft Dassault Falcon 2000LX ISTAR (credit: DLR)

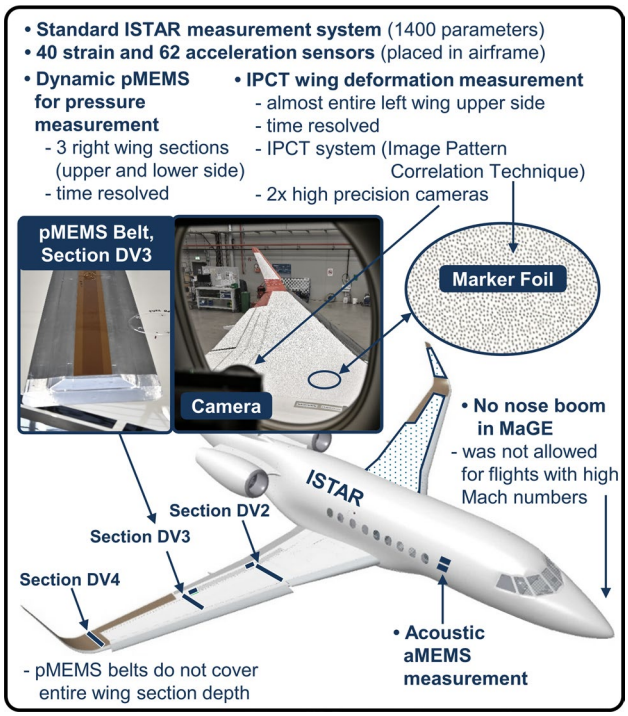

Fig. 3 HighFly flight campaign MaGE – ISTAR instrumentation

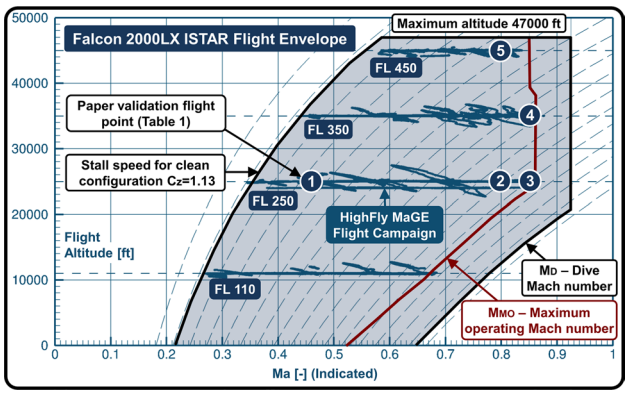

Fig. 4 HighFly flight campaign MaGE in ISTAR flight envelope

under real flight conditions for the first time at DLR. With this high-quality flight test data, the validation of simulation models for virtual flight testing and the quantification of numerical uncertainties are carried out. Especially valuable here are the in-flight measured data outside the normal operational range close to the edges of the flight envelope. The ongoing validation shows the accuracy and applicability limits of the current high-fidelity aeroelastic simulations in these regions. Furthermore, it provides best-practice approaches and shows efficiency, robustness, and procedural gaps.

1.4 Content of paper

The steady-state trimmed aeroelastic simulations of the ISTAR aircraft in the clean cruise configuration (retracted flaps and landing gear) are computed using the multidisciplinary process chains FSAerOpt and UltraFLoads. In the following section, these two process chains are briefly introduced together with ISTAR numerical models and simulations. More detailed descriptions of these numerical models and simulations were published in [17]. After that, the first comparisons of the steady-state trimmed fluid–structure coupled (CFD-CSM coupled) simulations with the measured values of five selected MaGE flight points are shown and discussed. The pressure distributions on three wing sections, trim variables, and elastic wing deformations are compared. Finally, several sensitivity studies of CFD geometries and meshes and different numerical parameters are presented.

Steady-state aeroelastic trimmed simulations (simulation of a symmetrical unaccelerated trimmed horizontal 1 g flight) serve as an initial solution for flexible dynamic maneuver simulations, which will be introduced together with their validation in future papers.

This paper does not describe in detail the experimental sensors (pMEMS and IPCT), such as their setup and calibration.

2 Simulation process chains, numerical models, and analyses of ISTAR

2.1 Simulation process chain FSAerOpt

The process chain FSAerOpt was developed in the CAS department (Center for Computer Applications in AeroSpace) of the DLR Institute for Aerodynamics and Flow Technology in Braunschweig, Germany. It was created mainly for MDO (Multidisciplinary Design Optimization) but can also be used only for MDA (Multidisciplinary Analysis). FSAerOpt performs steady-state trimmed CFD-CSM coupled simulations in the FlowSimulator software integration framework, which was jointly developed by DLR, Airbus, and ONERA [18, 19]. FSAerOpt uses MSC Nastran [20] as a structure solver and DLR TAU-Code [21] as a flow solver. The engine thrust can be considered by the force vector or CFD boundary conditions. The latter can be coupled with a thermodynamic engine model. The aircraft is trimmed by adjusting the angle of attack, engine thrust, and elevator deflection or horizontal tail plane (HTP) rotation. The process chain FSAerOpt can only calculate symmetrical steady-state flight cases, and only half the CFD geometry is used in simulations. More information about FSAerOpt can be found in [22, 23].

2.2 Simulation process chain UltraFLoads

The process chain UltraFLoads (Ultra Fidelity Loads) has been developed in the Loads Analysis and Aeroelastic Design department of the DLR Institute of Aeroelasticity in Göttingen, Germany. It is a Python-based MDA simulation software focusing on aeroelastic applications with high-fidelity methods such as MSC Nastran [20] as a structure solver and DLR TAU-Code [21] as a flow solver. It utilizes data objects and plugins of the FlowSimulator and its DataManager [18, 19]. UltraFLoads provides an outer scenario layer to the FlowSimulator ecosystem. In addition to steady-state elastic trim cases, dynamic maneuvers can be simulated by implementing unsteady structural modal analysis and flight dynamics calculations (rigid body motion). More detailed information about the architecture and the capabilities of UltraFLoads can be found in [24, 25], and three applications are presented in [26, 27].

Both process chains are used in the validation activities; however, the results presented in this paper are primarily calculated using FSAerOpt.

2.3 Numerical models and simulations of ISTAR

Figure 5 gives basic information about the individual numerical models and simulations of the ISTAR aircraft used in this paper, which are not described further in the text. Figures 6, 7, and 8 depict the CATIA CAD geometry for CFD, the ANSA CFD mesh, and the FE (Finite Element) NASTRAN structural model of ISTAR. Figure 9 shows the distribution of the aircraft masses in the FE structural model (operating empty, fuel, and cabin masses). As mentioned, more information about the individual models and simulations used in this paper can be found in [17].

CFD Geometry
- CATIA V5 model [28] (Figure 6), clean cruise configuration
- Delivered by Dassault Aviation and corrected by optical measurements
- Wings, fuselage, HTP, VTP, engine nacelles, pylons, flap track fairings, and pMEMs belts with additional details like cables
- No details such as antennas, sensors, lights, system inlets and outlets, and no enhanced flight vision camera fairing on the nose upper side
- Smooth surface: no rivets, embossing, and gaps, except for the ailerons
- Engine with one inlet surface with a spinner and one outlet surface

CFD Meshes
- ANSA meshes [29], unstructured mixed-element type (Figure 7)
- No. of grid points: 5 to 120 million (half configuration), y+_target=1 for the validation point with the highest Reynolds no., other validation points with lower Reynolds no. y+<1
- FSAerOpt simulations use the half configuration with a symmetry plane, UltraFLoads simulations use the full configuration which is created by mirroring the half mesh

CFD Simulation
- DLR TAU-Code [21] – cell-vertex finite volume solver, can solve the steady RANS and unsteady RANS equations (dual-time stepping)
- Compressible and viscous flow in fully turbulent regime
- In most cases: SA-neg one-equation turbulence model, second-order spatial discretization based on the scalar-dissipative central convection scheme and Green-Gaussian gradients for the viscous flux
- Implicit backward Euler time-stepping with symmetric forward-backward Gauss-Seidel iterations
- Powered engine with flow boundary conditions (inlet and outlet surface)

Flight Control Surface Modeling in CFD
- All primary flight control surfaces can be modeled: elevators, ailerons, rudder, and HTP (rotation)
- Simplified control surface deflection with user-defined blending areas (mesh morphing approach) [30]
- CFD volume mesh is deformed with the Radial Basis Function (RBF) mesh deformation [31]

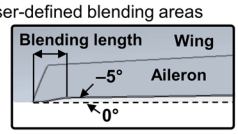

CSM Simulation
- FE software MSC NASTRAN [20], provided by DLR Inst. of Aeroelasticity
- FE NASTRAN structural model with 24863 nodes (Figure 8)
- FSAerOpt: linear static analysis SOL 101 (inertia relief -2)
- UltraFLoads: free-free modal analysis SOL 103 (up to 150 elastic modes)

Mass Distribution
- Distributed mass nodes in the structural NASTRAN model (operating empty, fuel, and cabin masses – Figure 9)
- Mass distribution can be adjusted by mass scaling with a Python tool

Engine Model
- DLRp2 thermodynamic performance model (DLR Performance Program [32]) of the PW308C engine delivered from the DLR Institute of Propulsion Technology in Cologne
- For a specified Mach number, altitude, and engine thrust, this model calculates, among other variables, the thermodynamic flow variables for the inlet and outlet surface of the powered engine in the TAU CFD domain

Fig. 5 Numerical models and simulations of ISTAR

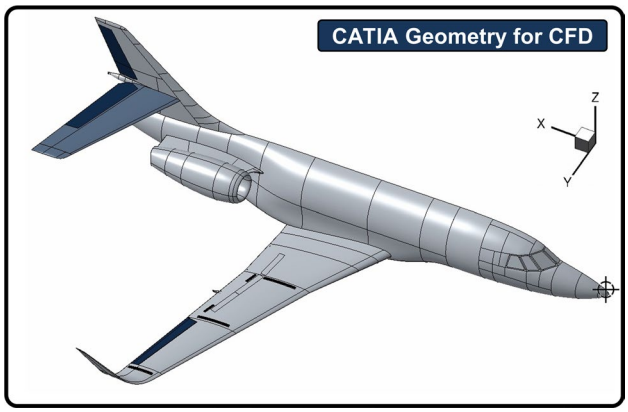

Fig. 6 ISTAR CAD geometry for CFD

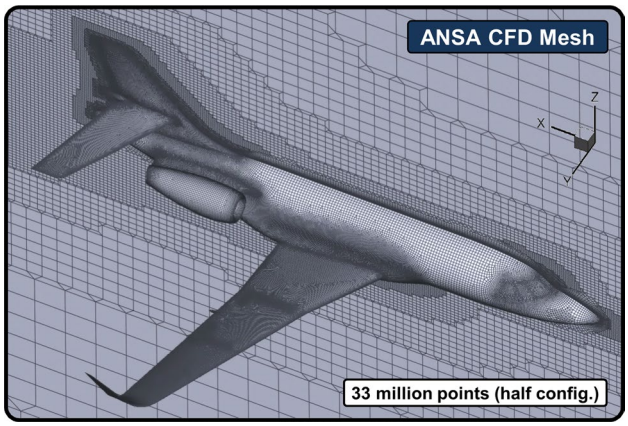

Fig. 7 Example of ISTAR CFD mesh

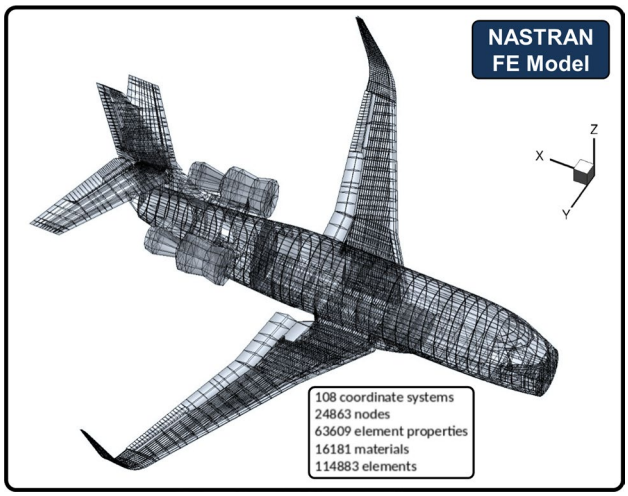

Fig. 8 ISTAR FE structural model

2.4 Process of steady-state CFD-CSM coupled trimmed simulation in FSAerOpt

In the previous section, the individual numerical models and simulations of the ISTAR aircraft are briefly introduced in isolation. In this section, their connections in the FSAerOpt simulation process are described.

Figure 10 schematically shows the FSAerOpt process of the steady-state CFD-CSM coupled trimmed simulation. The aeroelastic coupling (inner loop) starts with the aerodynamic CFD analysis (TAU-RANS). The aerodynamic loads are then interpolated from the CFD surface mesh to the load application nodes of the structural mesh (RBF weighted moving least squares method) and serve as boundary conditions for the structural analysis (NASTRAN SOL 101). The resulting elastic deformations are interpolated from the structural coupling nodes to the CFD surface mesh and propagated to the CFD volume mesh (RBF mesh deformation [31]). Then, the next iteration of the aeroelastic coupling begins. In the case of negative mesh cells after mesh

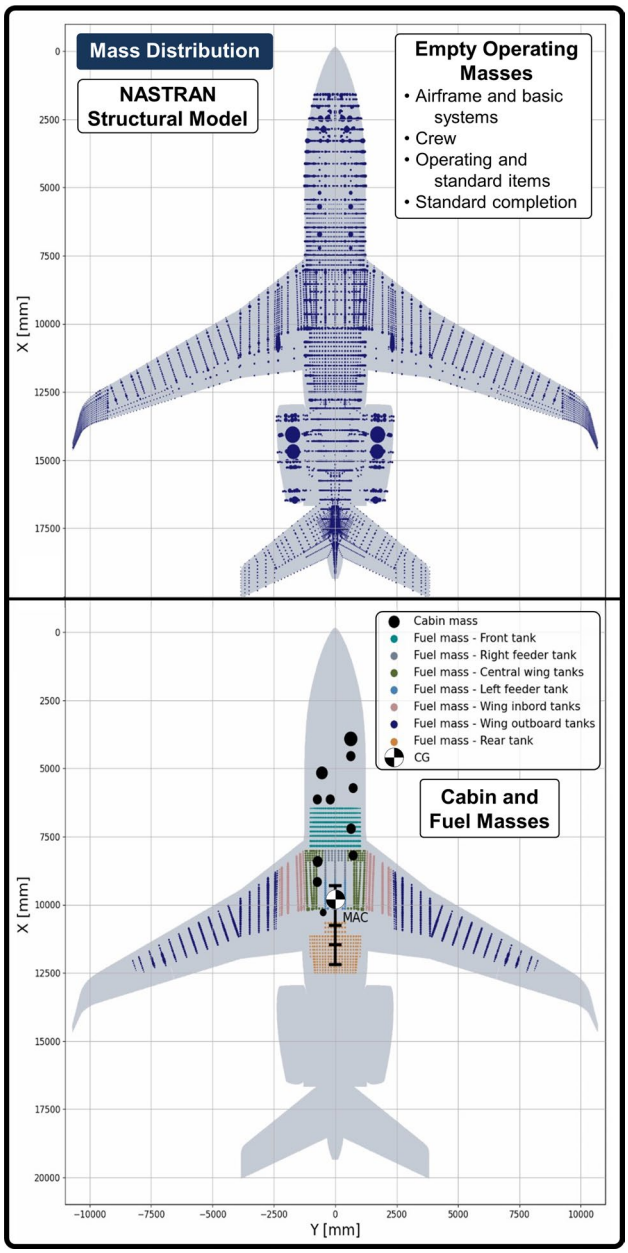

Fig. 9 Mass distribution in ISTAR structural model

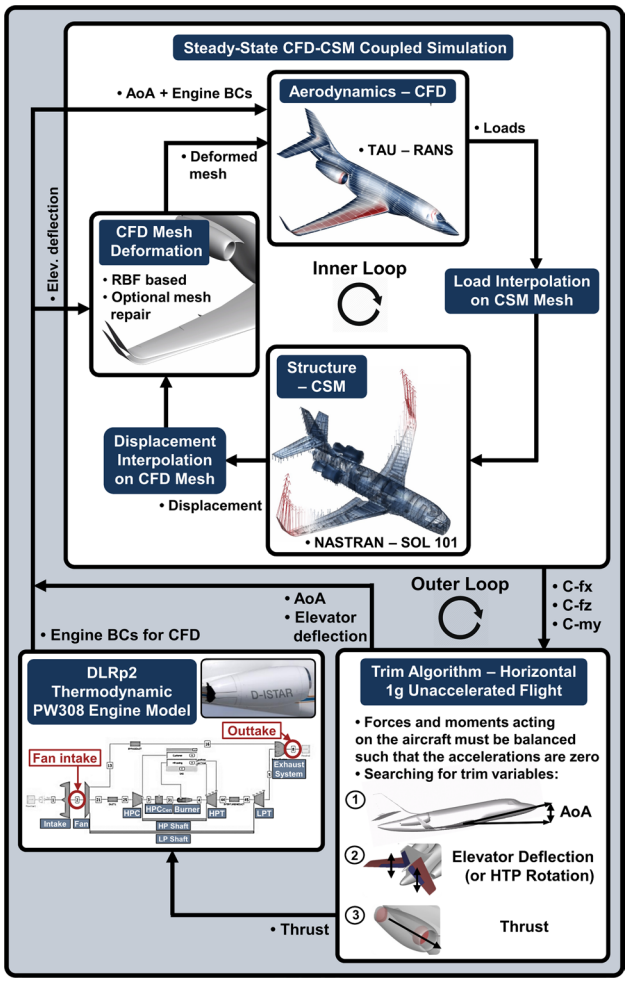

Fig. 10 Process of steady-state CFD-CSM coupled trimmed simulation in FSAerOpt

deformation, a mesh repair step can be locally applied with the linear elasticity method. This CFD-CSM iterative process is terminated when the user-defined criteria are met.

In the trim iterations (outer loop), the trim variables — the angle of attack (AoA), the elevator deflection (or HTP rotation), and the engine thrust — are changed until the translational acceleration X and Z and the pitch rotation acceleration Y are close to zero according to the user-defined criteria. This flight condition then represents symmetrical unaccelerated trimmed 1 g horizontal flight. The trim algorithm uses the Newton method to find the roots of the force and moment balances. The aerodynamic loads, gravitational force, and engine thrust are considered. The required Jacobian matrix is calculated at the beginning of the trim simulation using finite differences and updated during trimming using the Broydens-Bad method. The elevator is deflected using simplified control surface modeling with blending areas (see the aileron deflection in Fig. 5). During trimming, the DLRp2 engine model [32] receives the required thrust value from the trimming algorithm. The additional input parameters for this model are the flight altitude and the flight Mach number, which are held constant during trimming. The engine model calculates, among other variables, the thermodynamic flow variables for the powered engine's inlet and outlet surfaces in the TAU CFD domain.

The UltraFLoads process of steady-state CFD-CSM coupled simulation with trimming, which is not described here, uses methods similar to FSAerOpt, but there are some differences. For example, a reduced order model based on structural eigenvectors and eigenvalues (modal analysis SOL 103) can be used instead of linear static analysis (SOL

101). More information about the UltraFLoads processes can be found in [17, 24, 25].

All the presented simulations were computed on the DLR-HPC clusters CARA and CARO [33, 34]. For example, calculating one trimmed aeroelastic simulation with a CFD mesh of 44 million points (half configuration) takes approximately 24 h on 768 CPUs on CARA.

3 Simulation validation with MaGE flight test data

The first comparisons of the ISTAR numerical simulation results with the measured flight data and the official aircraft manufacturer data in the clean cruise configuration were presented in [17]. For example, the specific ranges for different altitudes and speeds between the FSAerOpt simulations and the aircraft flight performance manual [35] were compared (Fig. 11).

The presented paper shows new comparisons of the numerical simulation results of five flight points (steady-state aeroelastic trimmed simulations) with the flight data measured in the MaGE flight campaign.

3.1 Simulation flight input parameters and validation flight points

Before running each simulation, it is necessary to correctly set its flight input parameters, such as Mach number, flight altitude, aircraft gross weight, and center of gravity (CG) position, based on the measurements obtained during the flight tests. The incoming flow stream parameters are measured by the standard aircraft sensors (lower part of Fig. 12) and are corrected by correction models [36, 37]. The inaccuracy (uncertainty) of the measurements and the correction models must always be considered. In the MaGE flight campaign, it was not possible to use a nose boom (upper part of Fig. 12) with more accurate measuring sensors, including the measurement of the sideslip angle, which is otherwise unavailable on the ISTAR aircraft. Because of the lack of direct sideslip measurement and the estimated lower values of this angle, all the steady-state simulations are calculated as symmetrical (sideslip angle = 0º), including the rudder and ailerons without deflection. Symmetric simulations are also necessary for the FSAerOpt process chain, where only half of the configuration is simulated in CFD. The nose boom was not allowed due to the high flight Mach numbers in the MaGE flight campaign. In the meantime, a new ISTAR nose boom has been provided for future projects and is approved for the entire aircraft flight envelope.

The values of static and total pressure and total temperature from the aircraft standard sensors (lower part of

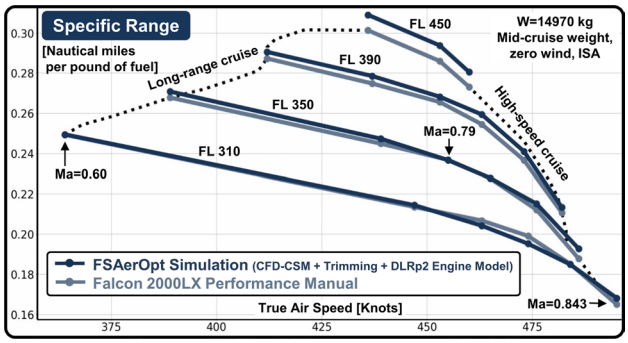

Fig. 11 ISTAR specific range – FSAerOpt simulation vs Falcon 2000LX performance manual (from [17])

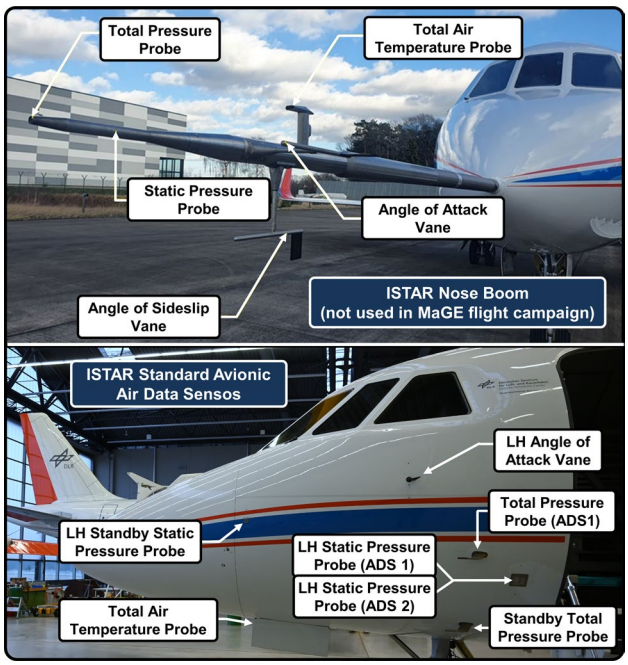

Fig. 12 ISTAR nose boom and standard avionic air data sensors (credit: DLR)

Fig. 12) are corrected using correction models provided by the DLR Institute of Flight Systems in Braunschweig using the ISTAR measurement data from the HighFly PID (Parameter Identification) flight campaign [36, 37]. The simulation input parameters of the inflow conditions (Mach number, static pressure, and density) can be calculated from these corrected values. The HTP rotation is set to the value from the flight computer in the simulations and the elevator deflection is a searched trim variable.

Before and after each flight of the MaGE campaign, the weight and X position of the CG of the aircraft with fuel and crew were measured on the ground via weight scales. The gross weight for the simulations is calculated as the preflight weight minus the fuel used (value from the flight computer) at a given flight time. The position X of the CG for the simulations is then determined from the CG weight diagram for

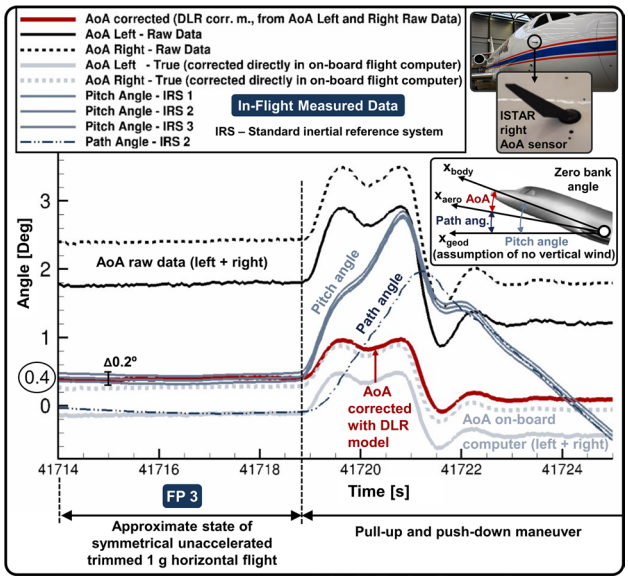

Fig. 13 In-flight measured data of FP 3 – angle of attack, pitch and path angles

a given gross weight (assumed to be more accurate than the CG position from the structural model). In addition, the mass distribution in the structural model can be adjusted in a simplified way by scaling the fuel mass nodes using the fuel levels of the different tanks (values from the flight computer) or by changing the mass distribution in the cabin (Fig. 9). The change in the X position of the CG caused by fuel displacement due to the aircraft pitch angle during a flight can be considered and determined using the manufacturer's diagram.

Also important are the flight parameter values against which the simulation results are compared, such as the angle of attack in a trimmed horizontal flight. For illustration, Fig. 13 shows the angle of attack and pitch angle curves from Flight Point 3 (FP 3) and the subsequent dynamic pull-up and push-down maneuver, whose simulation is not presented in this paper. It can be seen that, on the left, in the approximate trimmed 1 g level flight region (path angle of approximately 0º), the values of the corrected angle of attack (red curve) and pitch angle (three blue-gray curves)

Table 1 Validation flight points (FP)

Flight Point (FP)	1	2	3	4	5
Mach Number [-] (True)	0.459	0.787	0.829	0.827	0.782
Pressure Altitude [ft]	25 010	24 958	25 390	34 955	45 138
Reynolds Number (MAC based)	14.8M	25.5M	26.3M	19.4M	11.1M
Gross Weight [kg]	14 316	16 513	14 663	15 725	15 614
Lift Coefficient [-]	0.516	0.202	0.165	0.274	0.496
HTP Rotation [º]	-2.54	-0.29	0.00	-0.79	-2.08
CG X [m]	9.840	9.869	9.831	9.837	9.834
Flight State	Symmetrical unaccelerated trimmed horizontal 1 g flight				
Simulation Output	Trim variables: AoA, elevator deflection, and engine thrust				

from the aircraft inertial reference system (IRS) are both approximately 0.4º. However, it should always be considered that the corrected angle of attack measurement (red curve) may have an error of up to ± 0.3° (especially at higher sideslip angles). For comparison, in the European research project AWIATOR, the error in the angle of attack measurement on the Airbus A340-300 was also estimated to be ± 0.3º (Table 4 in [38]). The IRS measurements (pitch and path angles) are expected to be much more accurate, but no vertical wind is assumed to compare the measurement values of pitch angle (at path angle = 0º) with the angle of attack.

The trim variable thrust is not compared during validation due to the lack of direct measurements.

During the MaGE flight campaign, all trimmed flight points and dynamic maneuvers were flown manually in the calmest possible atmosphere without the use of an autopilot.

For the validation in the presented study, five flight points (unaccelerated trimmed 1 g horizontal flights) with three different Mach numbers and three different altitudes are selected. These five flight points are depicted in Fig. 4 in the ISTAR flight envelope and the relevant information is provided in Table 1.

3.2 Validation results – wing pressure distribution comparison

Before comparing the chordwise static pressure distributions between the simulations and the measurements, the right wing surface geometry is shown in more detail in Fig. 14 – A: fine optical measurement without the pMEMS sensor belts; B: coarse optical measurement with the pMEMS sensor belts; C to E: the CAD geometry for CFD simulations (upper and lower side) with the pMEMS sensor belts in the wing sections DV2, DV3, and DV4; and F and G: detail photos of the pMEMS belts. On the upper wing side, two shorter spanwise pMEMS belts are also located behind the spoilers (suitable for future validation of spoiler deflection simulations). Originally, pMEMS sensors were planned to be installed on more wing sections, including the tail surfaces; however, they could not be installed due to various restrictions. Hence, DV1 is missing in this paper. Figure 15 shows the ISTAR wing with the pMEMS sensors during a MaGE flight measurement.

In the first presented simulations, a geometry with the pMEMS belts and the cables without a detailed retracted slat geometry is used in CFD (Geom 3, 44 million points in the half configuration CFD mesh).

Figure 16 displays the first comparisons of the static chordwise pressure distributions (the wing sections DV2, DV3, and DV4) between the FSAerOpt simulations (blue curves) and the experimental pMEMS measurements (black points) for five steady-state trimmed flight points (FPs 1–5).

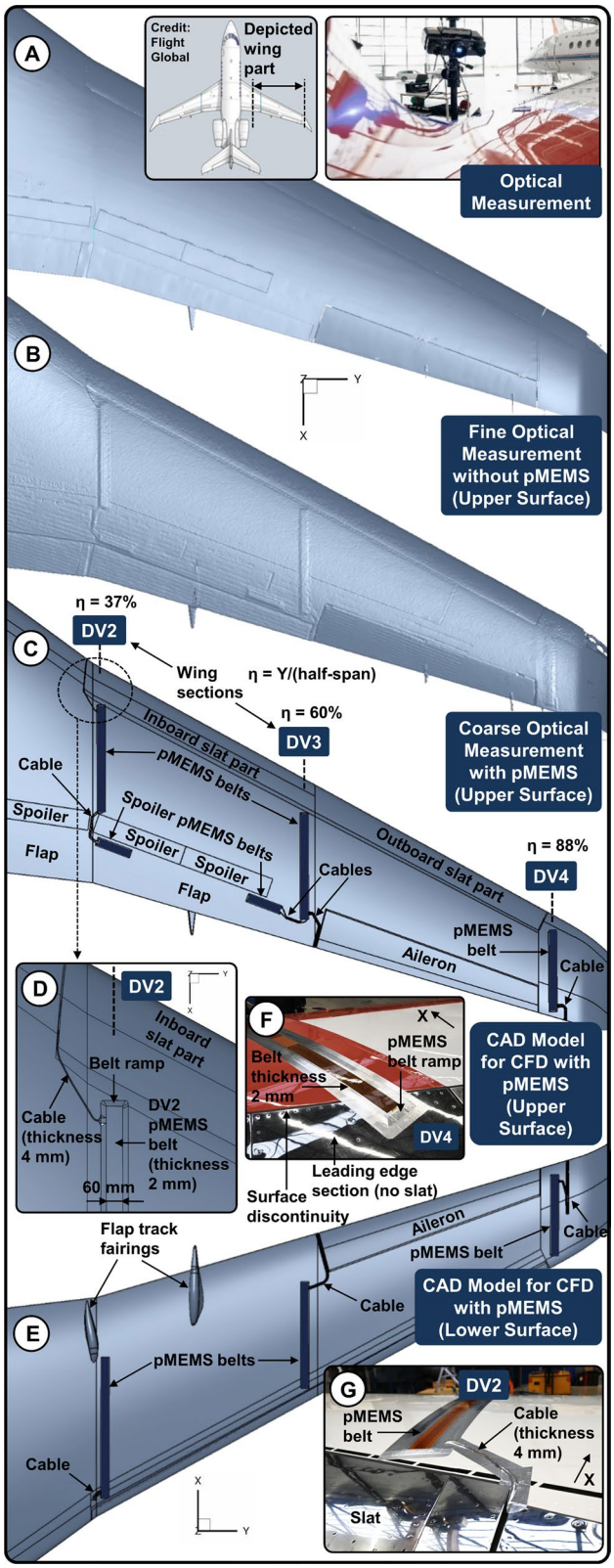

Fig. 14 ISTAR wing surface geometry with pMEMS belts

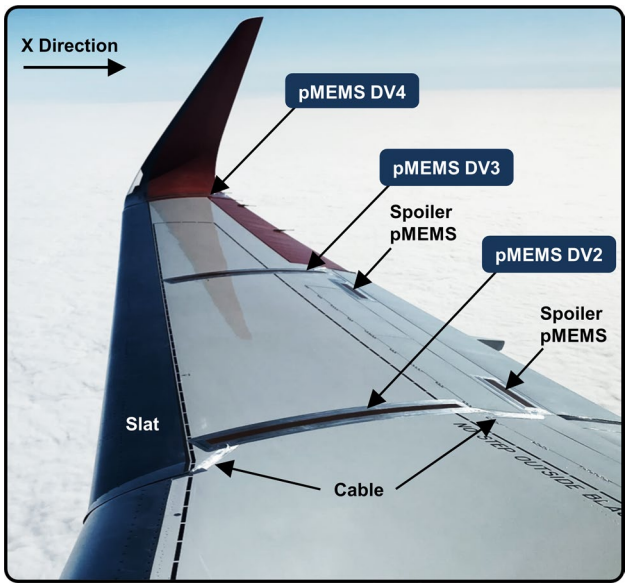

Fig. 15 ISTAR wing during MaGE flight measurement

From the measurements of the shorter spoiler pMEMS sensors, only one measurement point on the DV2 upper wing section is shown (see 1 in Fig. 16). The pressure distributions show local effects (local pressure peaks) at the beginnings and ends of all the pMEMS belts (see 2 in Fig. 16). This is caused by the leading and trailing ramps of the pMEMS belts with a thickness of 2 mm (see F in Fig. 14). This and other effects of geometric details on the pressure distributions (such as pMEMS cables) are discussed later.

The simulation static pressure values at a subsonic Mach number of 0.46 and flight level 250 (Fig. 16 – FP 1) agree very well with the measured experimental values. The largest deviations of this flight point are observed at DV4 (apparent when the diagrams are magnified), where the largest wing elastic deformation occurs, which is iteratively calculated in the coupled CFD-CSM simulation. Therefore, the most significant differences between simulations and measurements are generally expected in this outboard wing region. The flight shape twist inaccuracy in this elastic wing region can also indirectly affect the flow in the inboard part through the overall angle of attack, which is determined by the trim condition (1 g horizontal flight). When the diagrams of FP 1 are enlarged, a positive offset (in the downward direction) of approximately 100 Pa can be observed for most pMEMS measurement points compared to the simulation. This can be caused by the inaccurate setting of the simulation input parameters of the free-stream flow conditions or by a pMEMS measurement error (see 3 in Fig. 16).

Generally, a good correlation is observed in the transonic case at a Mach number of 0.79 and flight level 250 (Fig. 16 – FP 2). Some deviations are visible on the DV2 suction side. The suction peak in the front part of this section (see

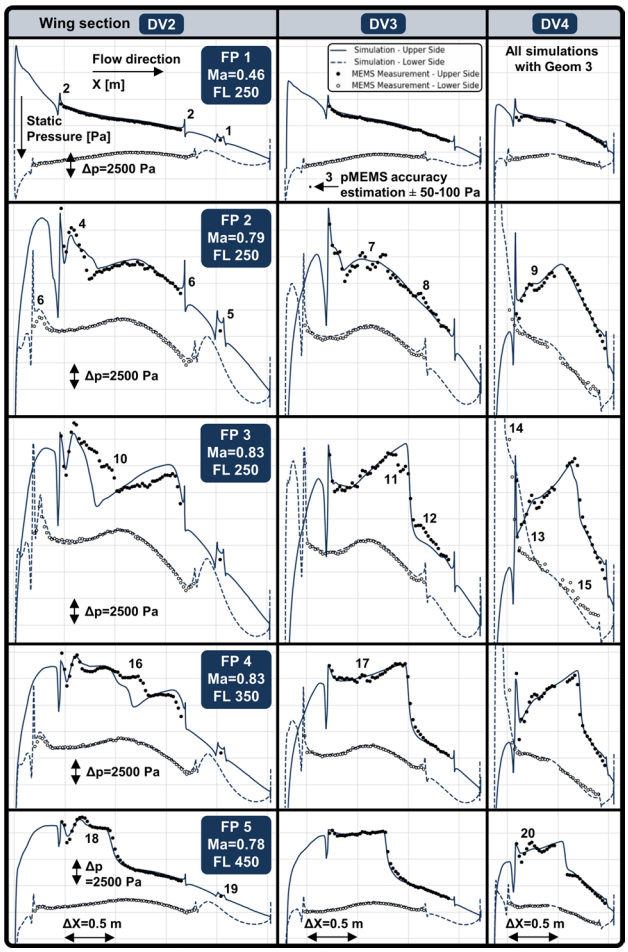

Fig. 16 Static pressure distributions at wing sections – simulation vs pMEMS flight measurement (FPs 1–5)

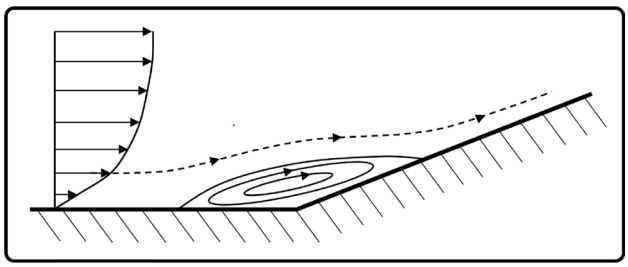

Fig. 17 Real viscous flow around sharp edge with boundary layer separation (schematic depiction)

4 in Fig. 16) is caused by the cable connecting the pMEMS belt (see G in Fig. 14). The simulation indicates a lower pressure than the measurement on the DV2 spoiler pMEMS belt (see 5 in Fig. 16). This could be caused by the fact that in real flow there are local boundary layer separations on sharp edges (Fig. 17), which reduce the curvature of the flow, i.e., weaker peaks in the pressure distribution. These local separations may not be captured in CFD simulations due to insufficient mesh resolution or inaccurate turbulence modeling. This simulation pressure overshooting can also be observed in other locations, for example, 6 in Fig. 16. It must also be taken into account that the geometry of the pMEMS belts and the cables is idealized in the CFD simulations and may deviate slightly from the real geometry; however, it is expected that these geometric deviations do not have a large effect on the pressure distribution. Further larger differences can be observed on the upper side of DV3 with a zigzag shape in the measurement (see 7 and 8 in Fig. 16). This could be attributed to the small spanwise surface waves visible on the measured wing geometry of the ISTAR aircraft (see the upper part of Fig. 18), which are missing in the CFD geometry (idealized smooth geometry shape). A test CFD geometry (without the pMEMS belts) is created, where surface waves comparable to the real geometry are approximately reconstructed in the two areas close to the DV3 wing section (the red ellipses in the middle part of Fig. 18). In the lower part of Fig. 18, the pressure distribution of the CFD simulation with reconstructed waves (red curve) is depicted, which is more similar to the pMEMS measurement. Missing local surface details and discontinuities in the CFD geometry, such as spanwise waves, may also cause local deviations at other locations and flight points, for example, point 9 in Fig. 16 at DV 4 (FP 2). This deviation can be attributed to the absence of the surface discontinuity behind the leading edge section of the wing (see F in Fig. 14). Similar deviations at this location of DV4 can also be observed at other flight points.

More significant deviations are visible in the case of transonic flight at a higher Mach number of 0.83 (close to the maximum operational Mach number) and flight level 250 (Fig. 16 – FP 3). The higher sensitivity of the flow to the geometry shape at high transonic speed can explain this. The largest differences are at the top of the DV2 wing section (see 10 in Fig. 16). Similar studies, as in the following Sect. 3.5 and 3.6, are performed for this flight point (different geometry details, CFD meshes, and numerical parameters) together with different reconstructions of the wing geometry from the optical measurement into the CAD model for the CFD simulation to investigate this deviation. These studies are not presented here and allow only a partial local convergence of the simulation values to the measurement (see example in Fig. 19). Two additional flight points with the same Mach number and flight altitude as FP 3 are also analyzed, showing the same deviation (not presented here). From these investigations, it is assumed that this more significant deviation between the measurement and the simulation is most likely due to some inaccuracy of the wing geometry in the CFD simulation, together with a possible combination of other uncertainties (inaccurate parameter settings), or due to the more complex geometry in the DV2 front part (the retracted slat, the cabel, and the pMEMS belt

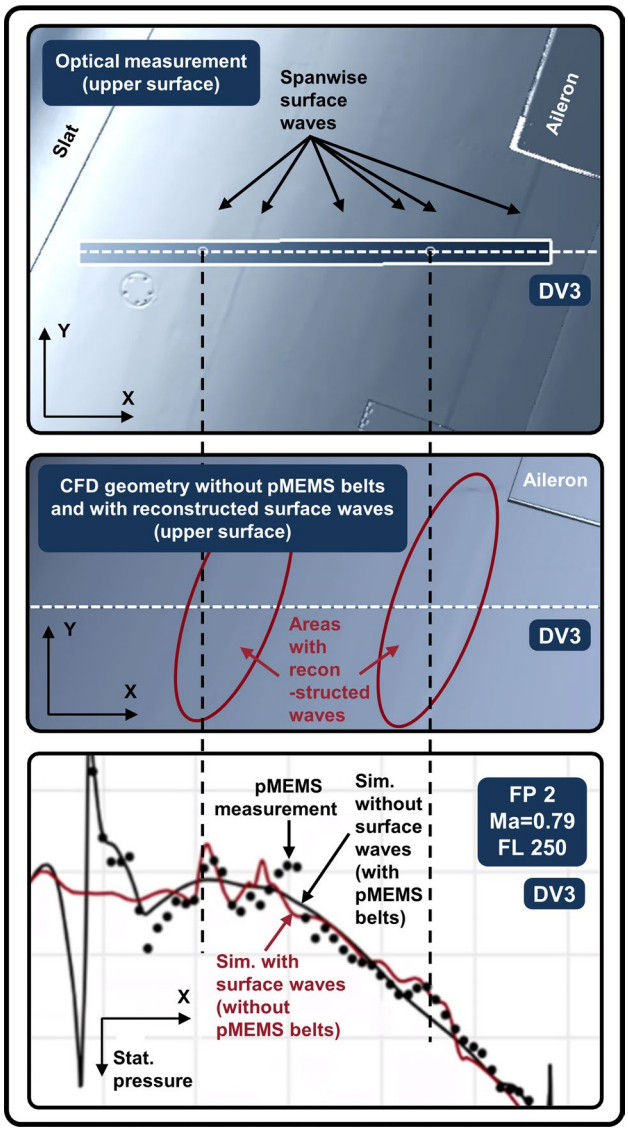

Fig. 18 Simulation pressure distribution with added spanwise surface waves (FP 2, DV3)

– see G in Fig. 14), which can cause an inaccurate CFD calculation of the flow with local boundary layer separations (e.g., turbulence modeling inaccuracy). Possible additional inaccuracies of the pMEMS measurements are also considered, for example, local detaching of the belt cover tape edge. Furthermore, on the suction side of DV3 at the measured pressure, there is a small compression before the shock wave compared to the simulation (see 11 in Fig. 16), which could be caused by a surface wave on the real geometry. The measured static pressure behind the shock wave is also lower than in the simulation (weaker shock wave). At this location, a spanwise wave is also missing in the CFD geometry (see 12 and 8 in Fig. 16). However, the simulation position of the shock wave correlates with the measurement. Another larger deviation can be observed on the pressure

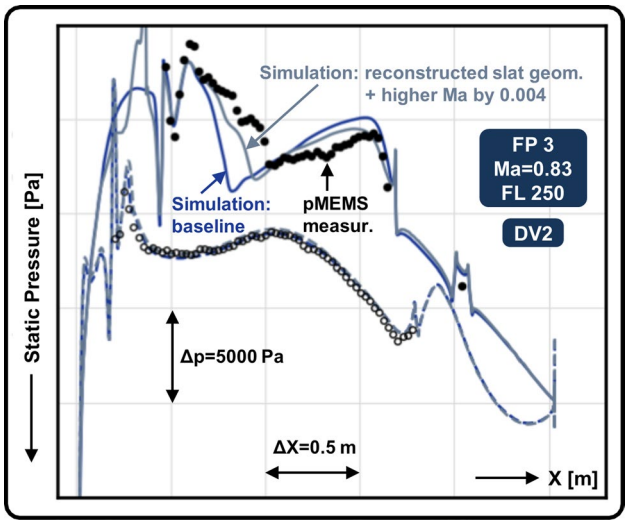

Fig. 19 Simulation pressure distribution with reconstructed slat geometry and higher Mach number by 0.004 (FP 3, DV2)

side of DV4. In the front part of this section, a boundary layer separation behind the shock wave occurs in the simulation (see 13 in Fig. 16 and 2 in Fig. 21). The simulation shock position agrees, however, with the measurement (see 14 in Fig. 16). The deviation behind the shock wave can be caused, for example, by an inaccurate CFD calculation (e.g., turbulence modeling), or CFD geometry. Furthermore, a missing wing outboard slat geometry in the retracted position can influence the flow in this area (see 1 in Fig. 21). It is worth noting that on the lower side of DV4, unsteady oscillations of the static pressure are evident in the measured pressure data in a time-lapse animation, which can represent a separation of the boundary layer (see 15 in Fig. 16).

For the flight point with a Mach number 0.83 and flight level 350 (Fig. 16 – FP 4), significant differences between the simulation and the measurement can again be observed on the upper side of DV2 (see 16 in Fig. 16). In contrast, the sections DV3 and DV4 show good correspondence. On the upper side of DV3, local deviations caused by missing surface waves can be observed again (see 17 in Fig. 16).

The simulation static pressure values of the flight point with a Mach number of 0.78 and flight level 450 (Fig. 16

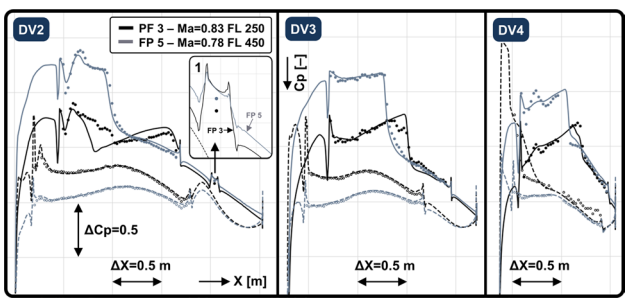

Fig. 20 Pressure coefficient distributions (FPs 3 and 5)

– FP 5) agree very well with the measured experimental values compared to FPs 3 and 4, including the upper side of DV2 (see 18 in Fig. 16) and the spoiler pMEMS at DV2 (see 19 in Fig. 16). Despite the lower Mach number than at FPs 3 and 4, a strong shock wave can be observed at FP 5 due to the higher angle of attack of the aircraft (higher flight altitude). The largest deviations of this flight point are at DV4 on the upper side (see 20 in Fig. 16). This can be attributed to the absence of the surface discontinuity behind the leading edge section of the wing in the CFD geometry mentioned earlier.

In addition to the different sensitivities of the flow to the geometry shape due to the different Mach numbers of FPs 1–5, different flight points also have different Reynolds numbers. Flight points with lower Reynolds numbers have larger boundary layer thicknesses and lower intensities of turbulent energy in the boundary layers. Turbulent boundary layers, in these cases, more effectively dampen the effects of small surface discontinuities, imperfections, and details on the external flow. Similarly, local surface details have a greater effect on the external flow in the front part of the wing where the boundary layer thickness is small (i.e., greater sensitivity).

Comparing the pressure distributions in Fig. 16 between FPs 3, 4, and 5, it is possible to observe different magnitudes of the local pressure peaks in the simulations at the beginnings and ends of the pMEMS belts, including the spoiler pMEMS belt on the DV2 upper side. This is mainly because Fig. 16 shows the static pressure distributions, i.e., the reaction of the static pressure on the same surface discontinuities is stronger at higher inflow dynamic pressure. For comparison, Fig. 20 shows the dimensionless pressure coefficient distributions[1] for FPs 3 and 5. Here, at point 1 (the spoiler pMEMS belt), smaller simulation pressure coefficient peaks are observed for FP 5 with a lower Reynolds number compared to FP 3, including better correspondence with the measurement.

Although the pMEMS belts are made of non-elastic material, their design allows them to exhibit flexibility in the primary direction, which is their length. Therefore, the installed pMEMS belts can follow the wing surface and should not suppress the local aerodynamic effects of small curvature changes of the wing in the belt's primary direction, as observed, for example, at points 7 and 8 in Fig. 16.

To summarize the pressure distribution comparisons in Fig. 16, despite specific differences, an acceptable correspondence between the simulations and the measurements can be observed in this initial simulation validation using the pMEMS measurements, which were performed for the first time at transonic speeds under real flight conditions at DLR.

Figure 21 shows the CFD wing flow topologies with surface pressure distributions for the five validation flight points presented.

3.3 Validation results – trim variable comparison

Figure 22 compares two trim variables (angle of attack and elevator deflection) between the simulations and the flight data. When comparing the angle of attack for all five flight points, a good correspondence is observed, except for FP 1, which has the most significant deviation of 0.29° (on the edge of the measurement accuracy range). For this flight point, the pitch angle value measured by the aircraft IRS system (at a path angle of 0º and with no vertical wind assumption) is closer to the simulation than the angle of attack measurement.

When comparing the elevator deflection, the largest deviations are at FP 3 (≈0.21°) and FP 4 (≈0.22°), where the simulations have higher negative values. These deviations are not considered significant. The other three flight points show perfect correspondence. The elevator deflection deviation can be caused by inaccurate CFD or CSM calculations (including inaccurate fuselage bending), inaccurate CG X position, elevator deflection with blending areas (resulting in relative imprecision of the simulation deflection value), or an inaccurate elevator deflection measurement value (calibrated on the ground).

3.4 Validation results – comparison of structural wing deformation

Figures 23 and 24 show the first comparisons of the flight wing elastic deformation between the IPCT measurement (Fig. 25) and the simulation (FSAerOpt – mirrored CFD result) for FPs 1 and 3. The estimated measurement uncertainty of the wing deformation defined by the IPCT setup (various sources, such as camera movement) increases with increasing distance from the cameras from 0.5 mm at $\eta = 28\%$ (Y position in the percentage of the half-span) to 6 mm at $\eta = 85\%$ for FP 1 and from 1 mm at $\eta = 28\%$ to 13 mm at $\eta = 85\%$ for FP 3. More information about the IPCT measurement technique can be found in [16].

In Figs. 23 and 24, the vertical deformation component (upper part of the figures) and flight shape geometries on the different upper wing sections (lower part of the figures) can be visually compared. For both cases, the simulations underestimate the elastic deformation (bending and twisting). A higher correlation between the measurement and the simulation is observed for FP 1, with a maximum visible deviation in the most outboard wing section of approximately 10 mm

[1] Difference between the local static pressure and the incoming flow static pressure relative to the incoming flow dynamic pressure.

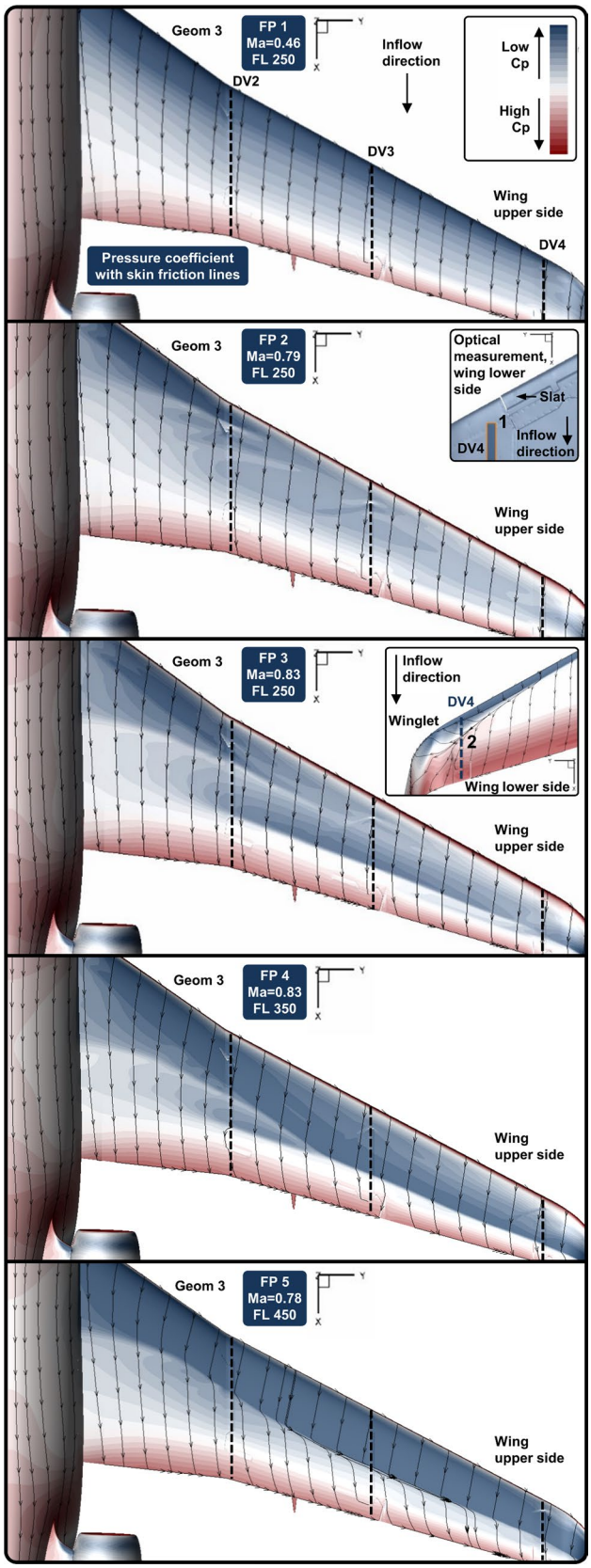

Fig. 21 CFD wing flow topology with surface pressure coefficient distribution (FPs 1–5)

FP 1 Ma=0.46 FL 250

Trim Variable	AoA [°]	Elev. defl. [°]
Simulation	4.14	-1.02
Flight Data	4.43 (4.20)	-0.95

FP 2 Ma=0.79 FL 250

Trim Variable	AoA [°]	Elev. defl. [°]
Simulation	0.81	0.09
Flight Data	0.82 (0.92)	0.12

FP 3 Ma=0.83 FL 250

Trim Variable	AoA [°]	Elev. defl. [°]
Simulation	0.49	-0.37
Flight Data	0.41 (0.44)	-0.16

FP 4 Ma=0.83 FL 350

Trim Variable	AoA [°]	Elev. defl. [°]
Simulation	1.10	-0.47
Flight Data	1.03 (1.17)	-0.25

FP 5 Ma=0.78 FL 450

Trim Variable	AoA [°]	Elev. defl. [°]
Simulation	2.84	-1.09
Flight Data	2.81 (2.85)	-1.06

Corrected AoA

IRS pitch angle at path angle=0° (assumption of no vertical wind)

Fig. 22 Trim variables – simulation vs flight measurement (FPs 1–5)

in the Z direction. The maximum visible deviation of FP 3 is in the most outboard wing section, approximately 25 mm in the Z direction (the inaccuracy of the measurement must be considered). For comparison, the elastic deformation of FPs 1 and 3 at the winglet is approximately 350–500 mm in the Z direction.

In Figs. 23 and 24, with the same axial scale, higher elastic bending and twisting are visible in FP 3 compared with FP 1. This is partially due to the fact that, at FP 3 with a higher Mach number, aerodynamic loads are centered more aft of the aeroelastic axis, leading to higher torsion moments.

3.5 Influence of CFD geometry details and CFD mesh resolution on results (FP 2)

Figure 26 shows the four different wing geometries used in the simulations. They differ only in the level of detail

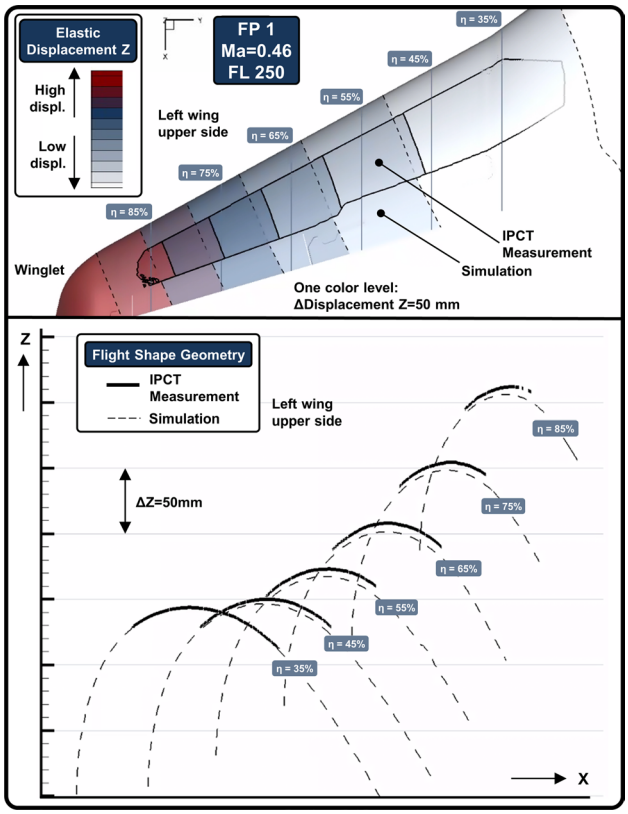

Fig. 23 Wing elastic deformation – simulation vs IPCT flight measurement (FP 1)

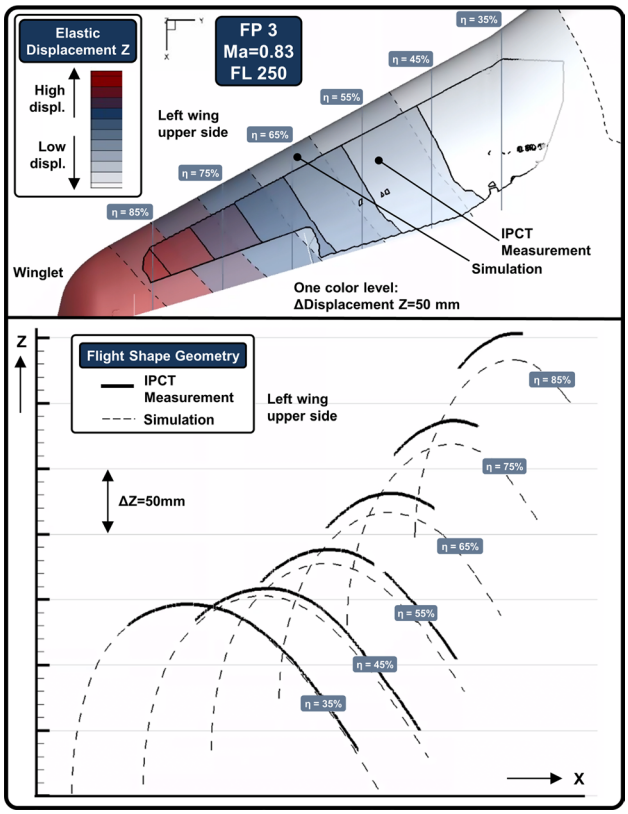

Fig. 24 Wing elastic deformation – simulation vs IPCT flight measurement (FP 3)

– Geom 1: the clean wing, Geom 2: the wing with the pMEMS belts, Geom 3: the wing with the pMEMS belts and the cables, Geom 4: the wing with the pMEMS belts, the cables, and the inboard slat part in the retracted position (the outboard slat part is not modeled).

Figure 27 displays a study of the effects of various CFD wing geometries (with similar CFD mesh resolutions) on the trim variables and simulation pressure distributions of FP 2. Only local effects on the pressure distributions can be observed and these geometric modifications do not lead to significant changes in the trim variables. This lower sensitivity enables the calculation of only the half configuration with the pMEMS belts and a symmetry plane instead of the entire asymmetric aircraft configuration with the pMEMS belts on the right wing and the left wing without these sensors. The effect of the pMEMS belts on the upper side of the wing can be seen at points A in the second row of Fig. 27. Furthermore, the cable effects are visible at points B in the third row. The effect of the more detailed geometry of the inboard slat part (retracted position with a 1.8 mm slat-wing step) is negligible (fourth row). In the diagram with Geom 4, four suction peaks are visible on the upper side of DV2 in the simulation – 1: a supersonic peak on the slat, 2: the slat-wing step, 3: the pMEMS belt, and 4: the cable. The details of the CFD simulation in this region are shown in Fig. 28.

Figure 29 shows the effect of the CFD mesh resolution on the trim variables and the wing pressure distributions of FP 2. Seven different CFD meshes (Geom 4, from 7.5 million points to 80 million points in the half configuration) are generated and computed. The mesh refinement change is performed via global scaling of the surface and volume mesh sources in the ANSA mesh generator. The

Fig. 25 IPCT marker foil on left wing of ISTAR

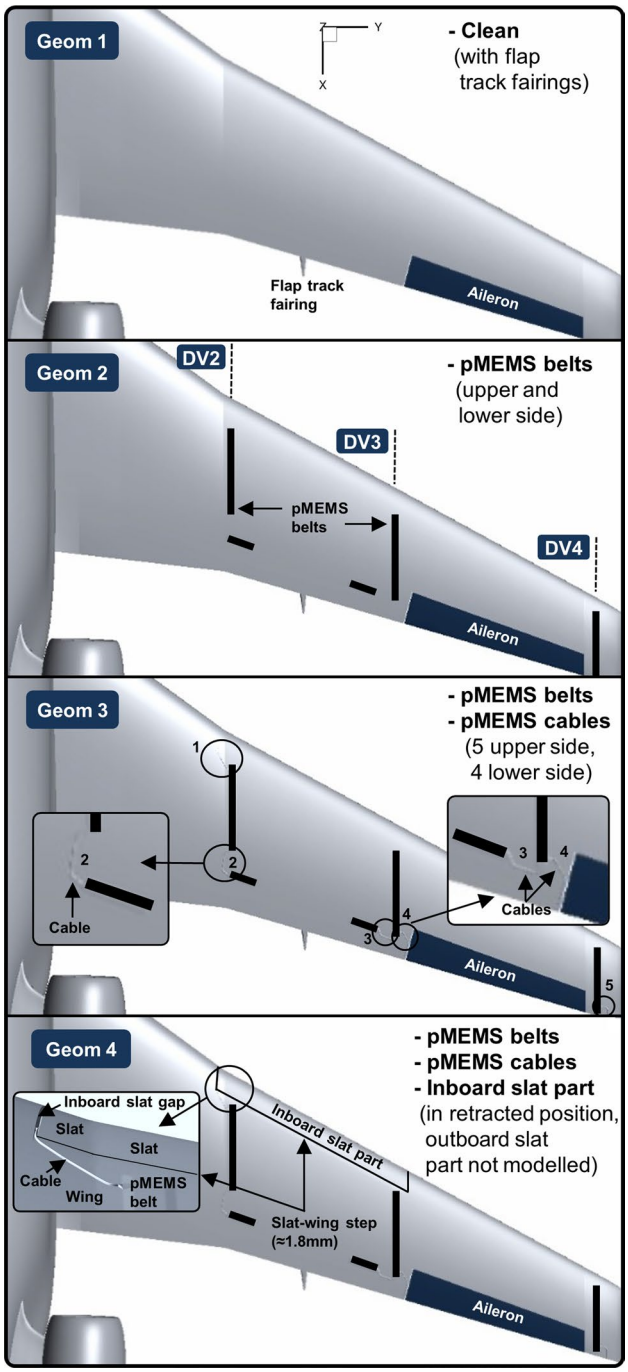

Fig. 26 CFD wing geometries with different levels of detail

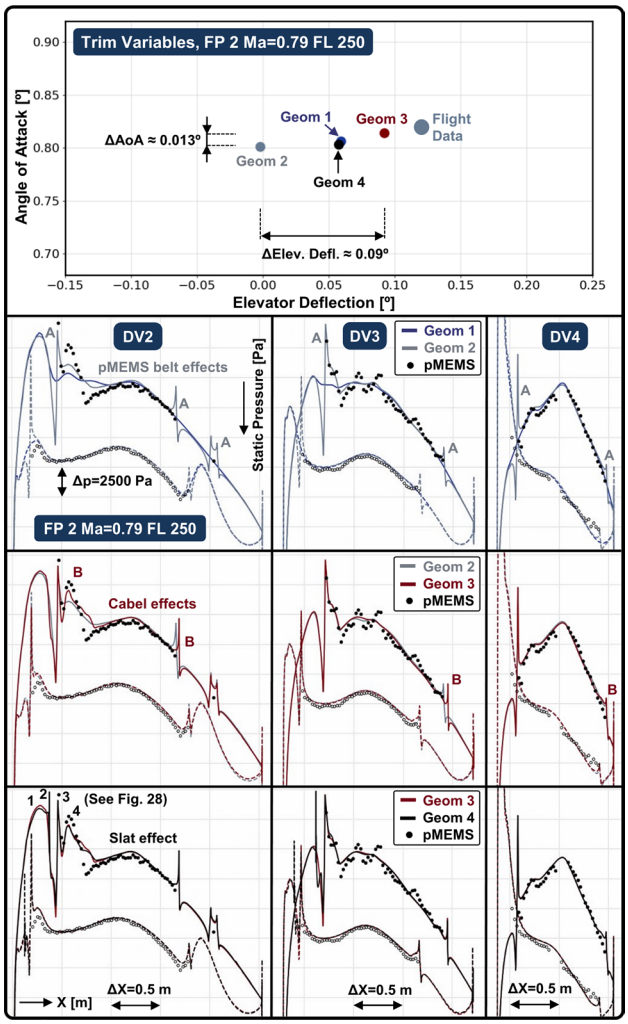

Fig. 27 Influence of CFD geometry details on results (FP 2)

prism layer parameters (targeted y+ = 1 and normal growth factor = 1.18) are held constant. A convergence study was first performed for the isolated rigid CFD simulation (with no coupling to CSM), where convergence was observed in lift, drag, and pitch coefficient during mesh refinement (not shown here). The mesh convergence study for the trimmed CFD-CSM simulation is presented in Fig. 29. Convergence can be observed during the mesh refinement for the trim variable engine thrust. For the angle of attack and the elevator deflection, convergence can only be partially observed. This is likely because the CFD-CSM coupling of the presented cases is not exactly the same, as it depends, among other things, on the number of points in the CFD surface mesh. From the diagrams in Fig. 29, it is evident that the mesh resolution has only a small effect on the trim variables and pressure distributions. However, it can be seen that the simulation elevator deflection of the finest mesh is closer to the flight data than the coarsest mesh.

3.6 Parameter variation study (FP 2)

This section presents a numerical parameter variation study for FP 2. Its purpose is to determine the sensitivity of the trim variables and the wing pressure distributions to the individual parameters and to compare them (also with Figs. 27 and 29). Figure 30 shows, besides the simulation reference case and the flight data, the following variations:

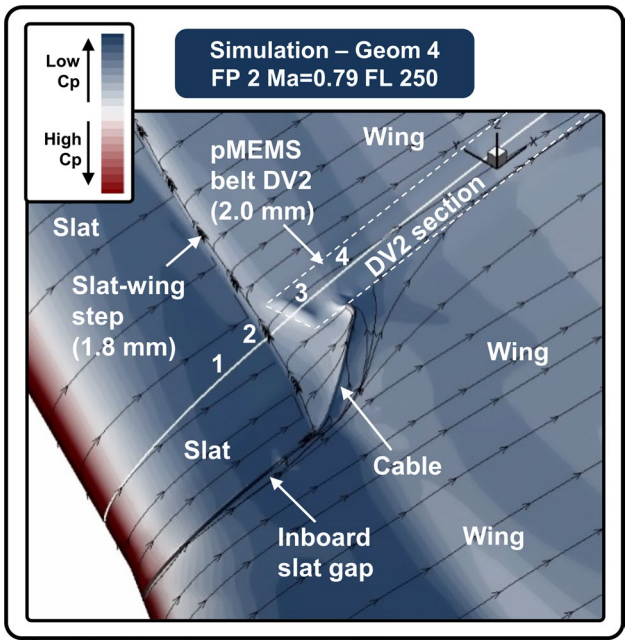

Fig. 28 Front part of DV2 – details of CFD simulation result (FP 2)

- computation with process chain UltraFLoads (UFL) with sideslip angles of zero and one degree
- variation of the Mach number (±0.01)
- variation of the flight altitude (±250 m)
- variation of the aircraft weight (±500 kg)
- variation of the position X of the CG (±1% of the mean aerodynamic chord)
- artificial scaling of the aerodynamic loads in the CSM Nastran calculation (simulation of structural elasticity change)
- thrust variation (investigates the effect of thrust variation on the flow around the wing and on the change in pitching moment and thus the change in the elevator deflection)
- simulation using the CSM model without fuel and cabin masses
- variation of the CFD parameters (spatial discretization and turbulence model)

Other parameters have been investigated, such as the CFD-CSM coupling parameters and the CFD mesh deformation parameters, which are not shown here. The influence of these parameters is not significant (within the typical range of values), as previously presented in [17].

The diagram in Fig. 30 shows the varying sensitivities of the trim variables to different parameters, e.g., a lower sensitivity to the thrust variation and the turbulence model. The latter has a more significant effect on the aircraft drag, as well as the trim variable thrust (not shown here). The

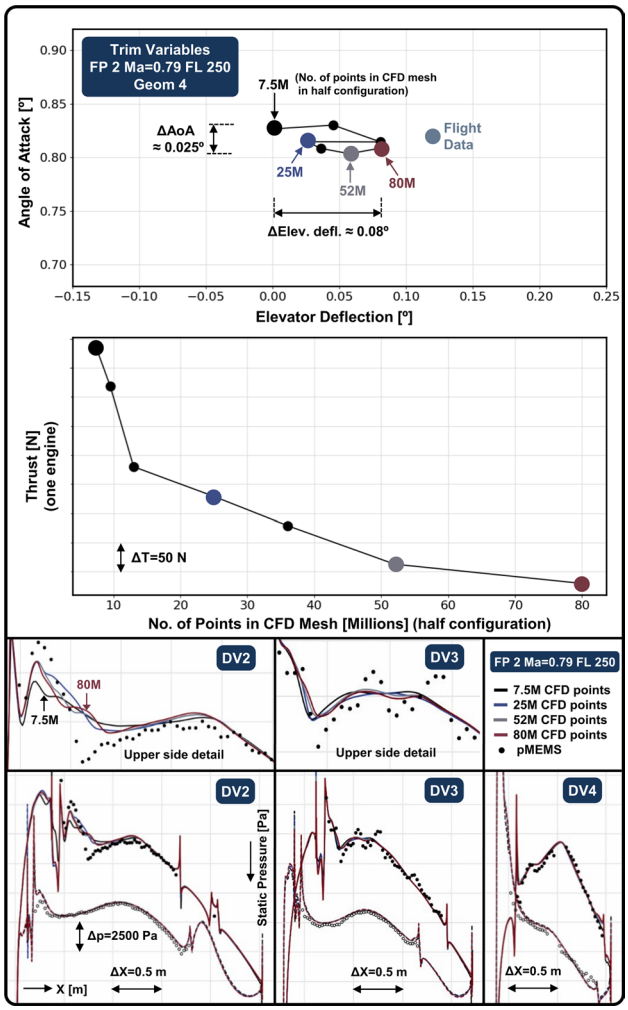

Fig. 29 Influence of CFD mesh resolution on results (FP 2)

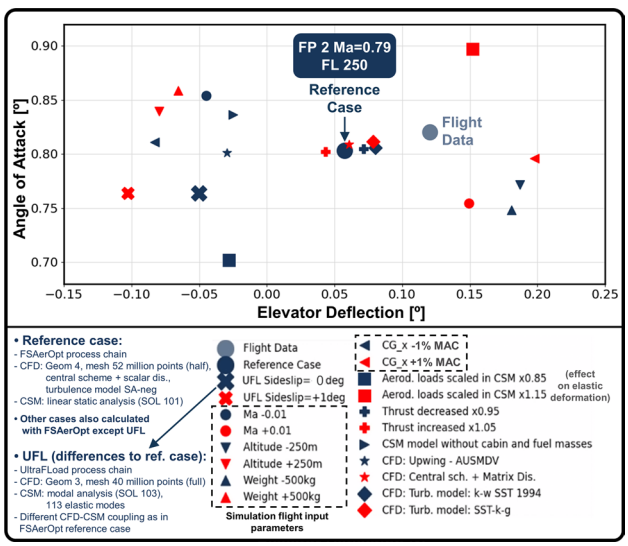

Fig. 30 Parameter variation study (FP 2)

difference between the FSAerOpt (reference case) and UltraFLoads (UFL) simulation is apparent. The main differences between these two simulations are described in Fig. 30, bottom left. Note that the direct linear structural solver SOL101 with inertia relief is applied for FSAerOpt, whereas a reduced set of structural eigenvectors is used for the modal approach in UltraFLoads. A similar deviation between FSAerOpt and UltraFLoads in trimming variables was also observed in [17] (Fig. 17, Diagram 1).

Furthermore, the higher sensitivity in Fig. 30 can be observed in the following cases: the aerodynamic load scaling in the CSM model, the CSM model without fuel and cabin masses, and the variation in the simulation flight input parameters: Mach number, altitude, gross weight, and position X of the CG (the latter has a larger influence on the elevator deflection). To accurately compare the sensitivities of these simulation flight input parameters with each other, it is necessary to know the ranges of absolute measurement errors, which are currently unknown for all parameters.

For a proper uncertainty study, it would be necessary to calculate various combinations of all the parameters. However, it is not the purpose of this paper to provide a comprehensive uncertainty quantification of numerical simulations and experimental measurements.[2]

It is also necessary to consider that the elevator is deflected in the simulations with the blending areas (see the aileron deflection in Fig. 5). Varying the blending length changes the deflection effectiveness. Some simulation studies should be conducted to investigate the effect of flight control surface deflections with and without the mesh morphing approach (with and without blending) on determining the optimal blending length, which is especially important for dynamic maneuver simulations with high flight control surface deflection values. The accuracy of the elevator deflection value from the flight measurement is also unknown.

Figure 31 shows the effect of changing the simulation free-stream Mach number on the static pressure distribution as an example of all the different parameter variations.

It is necessary to consider that in other flight cases with higher Mach numbers, higher angles of attack, higher load factors, and boundary layer separations, variations in different CFD meshes, geometry details, and numerical parameters may exhibit higher sensitivity to pressure distributions and trim variables than in this chapter.

[2] The process of characterizing all major sources of uncertainty in numerical models and analysis, and experimental measurement (identification, characterization, propagation, aggregation, and analysis).

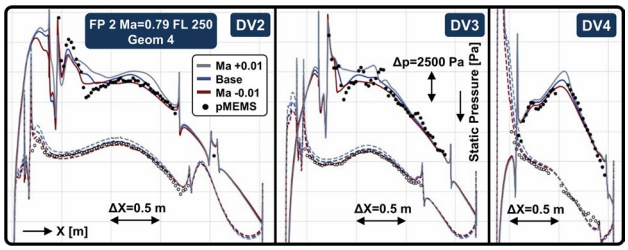

Fig. 31 Variation of simulation flight Mach number – wing static pressure distributions (FP 2)

4 Conclusion and outlook

This paper presents the first validation of steady-state trimmed aeroelastic simulations using experimental data measured on the DLR aircraft Falcon 2000LX ISTAR in the clean cruise configuration during the HighFly flight campaign MaGE. Five flight points (FPs 1–5) with three different Mach numbers and three different flight altitudes are selected for the validation.

Some missing wing details in the CFD geometry, compared to the measured ISTAR geometry, such as spanwise surface waves, result in small local deviations between the measurements and the simulations in the static pressure distributions. At a subsonic Mach number of 0.46 and flight level 250 (FP 1), a perfect agreement is observed between the pMEMS pressure measurement and the simulation. The flight point with a Mach number of 0.79 and flight level 250 (FP 2) shows good correspondence. The largest deviations appear in the flight cases at a higher Mach number of 0.83 and flight levels 250 and 350 (FPs 3 and 4). The higher flow sensitivity to the geometry shape at high transonic speed can explain this. It is assumed that the depicted significant pressure deviations between the measurement and the simulation (upper side of the DV2 wing section) are most likely due to inaccuracies in the wing geometry of the CFD simulation, together with a possible combination of other uncertainties (e.g., inaccurate CFD calculation or parameter settings). In contrast, at a Mach number of 0.78 and flight level 450 (FP 5), where a strong shock wave is present due to the higher angle of attack, the simulation pressure distributions agree very well with the pMEMS measurement. The presented pressure distribution deviations (mainly DV2 upper side at FPs 3 and 4) will be investigated in future validation activities.

In the next section, the trim variables (angle of attack and elevator deflection) from the simulations are compared with the flight measurements. The differences in the angles of attack for all five flight points lie within the accuracy range of the measurement. The deviations in the elevator deflection correspond reasonably well. In the comparison of elastic wing deformation for two flight points (FPs 1 and

3), the simulations slightly underestimate elastic bending and twisting compared with the flight IPCT measurement. Furthermore, the influence of the CFD geometry details and the mesh resolution on the simulation results is investigated for FP 2. Only local effects on the pressure distributions can be observed and these variations of the CFD geometry and mesh do not lead to significant changes in the trim variables. Finally, a numerical parameter variation study for FP 2 is shown. Its purpose is to determine the sensitivity of the trim variables and the wing pressure distributions to the individual parameters and to compare them.

In future validation activities with flight data from the MaGE flight campaign, other steady-state trimmed flight points could be investigated. The next step is to simulate dynamic maneuvers such as pull-up and push-down or bank-to-bank maneuvers, which will be shown together with their validation in future papers. Additionally, transonic buffet onset could be simulated for different flight cases and compared with the aircraft flight manual or with flight data from the MaGE flight campaign, where a light buffet occurred during some maneuvers.

In future DLR projects on validating virtual flight tests and certification by analysis, the aircraft Falcon 2000LX ISTAR should be used again. The nose boom equipped with more accurate measuring sensors, and additional pMEMS sensors located on both sides of the aircraft, including the tail surfaces, could be used for flight measurements. The measured wing geometry should be more accurately reconstructed into the CAD model used for CFD, which could include more wing details, such as small spanwise surface waves. In the HighFly project, ground vibration tests (GVTs) and flight vibration tests (FVTs) were performed with the ISTAR aircraft. Their results validated the currently used FE model. A new updated FE structural model of ISTAR could be used in future projects, which could make aeroelastic simulations more accurate.

DLR is continuously working on various projects to improve and refine experimental flight measurement methods, such as pMEMS or IPCT, as well as the calibration of aircraft avionic air data sensors.

On the side of numerical methods and multidisciplinary simulation process chains, developers continue to work on implementing new features and improving the efficiency of the simulation process. In future projects, the following features could be implemented in simulations of virtual flight tests: automatic mesh adaptation, laminar-turbulent transition models, nonlinear structural calculations, and more advanced flight control surface deflections, such as the sliding interface approach. It is planned to replace the DLR TAU-Code with the next-generation CFD solver CODA [39], which is jointly developed by DLR, Airbus, and ONERA.

The validation of high-fidelity aeroelastic simulations with flight test data is challenging and complex. This is due to several mutually coupled simulation disciplines, different numerical models, and a large number of individual numerical parameters. Additionally, it is also complex because of flight measurements under real atmospheric conditions with real aircraft with all geometric details, such as gaps, roughnesses, waviness, sensors, and antennas,[3] in this validation project as well with the pMEMS belts and cables; and also because of inaccuracies and uncertainties in the measuring sensors. All these uncertainties and errors appear simultaneously in numerical simulations and flight measurements. Thus, it is difficult to classify different error and inaccuracy sources separately. Therefore, it is necessary to continue further validation activities for different aircraft configurations and flight cases, using both flight measurement data and wind tunnel measurement data, to confirm the sufficient accuracy and level of fidelity of the virtual flight test simulations, especially outside the normal operational range, close to the edges of the flight envelope.

Acknowledgements The results presented in this paper are part of the DLR internal project HighFly (High Speed Inflight Validation). The authors gratefully acknowledge the scientific support and HPC resources provided by the German Aerospace Center (DLR). The HPC system CARA is partially funded by "Saxon State Ministry for Economic Affairs, Labour and Transport" and "Federal Ministry for Economic Affairs and Climate Action". The HPC system CARO is partially funded by "Ministry of Science and Culture of Lower Saxony" and "Federal Ministry for Economic Affairs and Climate Action".

Author contributions M.B. wrote the main manuscript text with figures. All authors reviewed the manuscript. J.F. helped with calculations with UltraFLoads process chain. P.M. supplied pMEMS data, helped with the CAD geometry preparation. T.K. supplied IPCT data.

Funding Open Access funding enabled and organized by Projekt DEAL.

Data availability No datasets were generated or analysed during the current study.

Declarations

Conflict of interest The authors declare no competing interests.

[3] Modern aircraft wings generally have higher surface accuracy and fewer discontinuities compared to older designs. Thanks to advanced manufacturing technologies and the use of composite materials, their surfaces are smoother, with fewer joints, gaps, and irregularities. Further improvements are expected in the future.

References

1. German Aerospace Center (DLR): Simulation Based Certification. https://www.dlr.de/en/research-and-transfer/projects-and-missions/simulation-based-certification Accessed 24 February 2025
2. American Institute of Aeronautics and Astronautics: Recommended Practice: When Flight Modelling Is Used to Reduce Flight Testing Supporting Aircraft Certification (AIAA R-154-2021). https://doi.org/10.2514/4.106231
3. Mauery, T., and issuing body Langley Research Center: : Guide for Aircraft Certification by Analysis. Hampton, Virginia: National AeronauticsSpace Administration, Langley Research Center, (2021). https://ntrs.nasa.gov/api/citations/20210015404/downloads/NASA-CR-20210015404%20updated.pdf Accessed 24 February 2025
4. Airbus: Test and certification. https://www.airbus.com/en/products-services/commercial-aircraft/the-life-cycle-of-an-aircraft/test-and-certification Accessed 24 February 2025
5. Roskam, J.: Airplane Design Part VIII: Airplane Cost Estimation Design Develop-ment and Manufacturing and Operating. Darcorporation (1990)
6. Collar, A.R.: The expanding domain of aeroelasticity. J. Royal Aeronaut. Soc. **50**(428), 613–636 (1946). https://doi.org/10.1017/S0368393100120358
7. Rudnik, R., Reckzeh, D., Quest, J.: HINVA - High lift INflight VAlidation - Project Overview and Status. In: 50th AIAA Aerospace Sciences Meeting (2012). https://doi.org/10.2514/6.2012-106
8. German Aerospace Center (DLR): Airbus A320-232 D-ATRA. https://www.dlr.de/en/research-and-transfer/research-infrastructure/research-aircraft-fleet/airbus-a320-232-d-atra Accessed 24 February 2025
9. Görtz, S.: Virtual Aircraft Technology Integration Platform - Results of DLR's Project VicToria. In: 32nd Congress of the International Council of the Aeronautical Sciences (ICAS (2021)
10. Ritter, M., Feldwisch, J.M., Voss, A., Kirmse, T., Reimer, L., Heinrich, R.: Comparison of Flight Test Data and Aeroelastic Simulation Results for DLR's Research Aircraft ATRA. In: Int. Forum Aeroelasticity Struct. Dynamics 13–17 (2022). June 2022, Madrid, Spain.
11. DLR Institute of Aerodynamics and Flow Technology: HighFly - Aerodynamics, aeroelasticity, structures and propulsion on the ISTAR research aircraft. https://www.dlr.de/en/as/research-and-transfer/projects/highfly Accessed 24 February 2025
12. German Aerospace Center (DLR): ISTAR Dassault Falcon 2000LX D-BDLR. (2025). https://www.dlr.de/en/research-and-transfer/research-infrastructure/research-aircraft-fleet/istar-dassault-falcon-2000lx-d-bdlr Accessed 24
13. German Aerospace Center (DLR): DLR conducts vibration tests on ISTAR. https://www.dlr.de/en/latest/news/2021/03/20210702_vibrating-research-aircraft Accessed 24 February 2025
14. German Aerospace Center (DLR): Four hundred flight manoeuvres with ISTAR advance its digital twin. (2025). https://www.dlr.de/en/latest/news/2023/02/four-hundred-flight-manoeuvres-with-istar-advance-its-digital-twin Accessed 24
15. Raab, C., Rohde-Brandenburger, K.: Dynamic flight load measurements with MEMS pressure sensors. CEAS Aeronaut. J. **12**, 737–753 (2021). https://doi.org/10.1007/s13272-021-00529-3
16. Kirmse, T., Boden, F., Meyer, R., Philipp, F.: Wing deformation measurements for manoeuvres of high load at the Airbus A320 DLR-ATRA by means of Image Pattern Correlation Technique. In: EUROPEAN TEST AND TELEMETRY CONFERENCE Proceedings Online, Pages 1–6. European Test and Telemetry Conference - Virtual, 2021-06-15–2021-06-16, TOULOUSE - France
17. Bauer, M., Feldwisch, J.M.: High-Fidelity multidisciplinary maneuver simulations of the Falcon 2000LX ISTAR. CEAS aeronaut J (2025). https://doi.org/10.1007/s13272-025-00849-8
18. Meinel, M., Einarsson, G.: The FlowSimulator framework for massively parallel CFD applications. PARA (2010). (2010)
19. Reimer, L., Heinrich, R., Geisbauer, S., Leicht, T., Görtz, S., Ritter, M., Krumbein, A.: Virtual Aircraft Technology Integration Platform: Ingredients for Multidisciplinary Simulation and Virtual Flight Testing. In: AIAA Scitech 2021 Forum. 11–15 & 19–21 January 2021. https://doi.org/10.2514/6.2021-1202
20. Hexagon, M.S.C., Nastran: https://hexagon.com/de/products/product-groups/computer-aided-engineering-software/msc-nastran Accessed 25 August 2023
21. Kroll, N., Langer, S., Schwöppe, A.: The DLR Flow Solver TAU – Status and Recent Algorithmic Developments. In: 52th AIAA Aerospace Sciences Meeting (2014). https://doi.org/10.2514/6.2014-0080
22. Merle, A., Ronzheimer, A., Bekemeyer, P., Görtz, S., Keye, A., Reimer, L.: Gradient-based Optimization of a flexible long-range transport Aircraft using a high-dimensional CAD-ROM Parameterization. In: DLRK 2018 - Deutscher Luft- und Raumfahrtkongress, 04–06 September 2018, Friedrichshafen (2018)
23. Merle, A., Stück, A., Remke, A.: An Adjoint-based Aerodynamic Shape Optimization. In: 35th AIAA Applied Aerodynamics Conference (2017). https://doi.org/10.2514/6.2017-3754
24. Feldwisch, J.M., Reimer, L., Ritter, M.: UltraFLoads - A Framework For High-Fidelity Loads Computations. In: DLRK 2021 - Deutscher Luft- und Raumfahrtkongress, 31 – 02 August-September 2021, Bremen (2021)
25. Feldwisch, J.M., Bauer, M.: UltraFLoads: A simulation suite and framework for High-Fidelity flight loads. Aerospace. **10**, 273 (2023). https://doi.org/10.3390/aerospace10030273
26. Feldwisch, J.M., Schulze, M.: High-Fidelity Aeroelastic Loads Calculation for a Transport Aircraft Configuration Including Pitch and Roll Maneuvers. In: Dillmann, A., Heller, G., Krämer, E., Wagner, C. (eds) New Results in Numerical and Experimental Fluid Mechanics XIII. STAB/DGLR Symposium 2020. Notes on Numerical Fluid Mechanics and Multidisciplinary Design, vol 151. Springer, Cham. https://doi.org/10.1007/978-3-030-79561-0_50
27. Zimmer, M., Feldwisch, J.M., Ritter, M.: Coupled CFD-CSM Analyses of a Highly Flexible Transport Aircraft by Means of Geometrically Nonlinear Methods. In: 19. International Forum on Aeroelasticity and Structural Dynamics, Madrid, 13–17 Juni 2022
28. Dassault Systems: Catia. https://www.3ds.com/products-services/catia/ Accessed 25 August 2023
29. BETA Simulation Solution: High Fidelity Automated CFD - Advanced Modeling: & Simulation Seminar Series. (2023). https://www.nas.nasa.gov/assets/nas/pdf/ams/2021/AMS_20210615_Skaperdas.pdf Accessed 22
30. Reimer, L.: User Guide of FSCtrlSurfDisplFieldGenerator. DLR Institue for Aerodynamics and Flow Technology, Braunschweig (2015)
31. Remke, A.: User Guide FS Mesh Deformation. DLR AS-CASE, Braunschweig (2020)

32. Becker, R.G., Reitenbach, S., Klein, C., Otten, T., Nauroz, M., Siggel, M.: An Integrated Method for Propulsion System Conceptual Design. In: Proceedings of ASME Turbo Expo 2015: Turbine Technical Conference and Exposition. https://doi.org/10.1115/GT2015-43251
33. German Aerospace Center (DLR): CARA. https://www.dlr.de/en/research-and-transfer/research-infrastructure/hpc-cluster/cara Accessed 24 February 2025
34. German Aerospace Center (DLR): CARO. https://www.dlr.de/en/research-and-transfer/research-infrastructure/hpc-cluster/caro Accessed 24 February 2025
35. Dassault Aviation: FALCON 2000EX EASy, FALCON 2000DX, FALCON 2000LX - Airplane Flight Manual. https://downloads.regulations.gov/FAA-2013-0862-0005/attachment_1.pdf Accessed 9 September 2023
36. Raab, C.: Dassault Falcon 2000LX ISTAR – Flight Data Gathering and DCC for System Identification – V1.00. DLR, Braunschweig (2022)
37. Raab, C.: Practical examples for the flight data compatibility check. CEAS Aeronaut. J. **14**, 1019–1033 (2023). https://doi.org/10.1007/s13272-023-00687-6
38. Keye, S.: Fluid-Structure coupled analysis of a transport aircraft and Flight-Test validation. J. Aircr. **48**(2), 381–390 (2011). https://doi.org/10.2514/1.C000235
39. Görtz, S., Leicht, T., Couaillier, V., Méheut, M., Larrieu, P., Champagneux, S.: CODA: A European Perspective for a Next-Generation CFD, Analysis and Design Platform. In: NATO Applied Vehicle Technology (AVT) Panel (2022)